3D printed sound-absorbing materials with double porosity[1]

Tomasz G. Zieliński[2]
Institute of Fundamental Technological Research, Polish Academy of Sciences
ul. Pawińskiego 5B, 02-106 Warsaw, Poland

Nicolas Dauchez
Thomas Boutin
Mikel Leturia
Alexandre Wilkinson
Universié de Technologie de Compiègne, Alliance Sorbonne Université, CNRS
Laboratoire Roberval, Centre de recherche Royallieu, CS 60319, 60203 Compiègne cedex, France

Fabien Chevillotte
François-Xavier Bécot
MATELYS – Research Lab
7 rue des Maraîchers (bâtiment B), F69120 Vaulx-en-Velin, France

Rodolfo Venegas
University Austral of Chile, Institute of Acoustics
P.O. Box 567, Valdivia, Chile

ABSTRACT

The paper shows that acoustic materials with double porosity can be 3D printed with the appropriate design of the main pore network and the contrasted microporous skeleton. The microporous structure is obtained through the use of appropriate additive manufacturing (AM) technology, raw material, and process parameters. The essential properties of the microporous material obtained in this way are investigated experimentally. Two AM technologies are used to 3D print acoustic samples with the same periodic network of main pores: one provides a microporous skeleton leading to double porosity, while the other provides a single-porosity material. The sound absorption for each acoustic material is determined both experimentally using impedance tube measurements and numerically using a multiscale model. The model combines finite element calculations (on periodic representative elementary volumes) with scaling functions and analytical expressions resulting from homogenization. The obtained double-porosity material is shown to exhibit a strong permeability contrast resulting in a pressure diffusion effect, which fundamentally changes the nature of the sound absorption compared to its single-porosity counterpart with an impermeable skeleton. This work opens up interesting perspectives for the use of popular, low-cost AM technologies to produce efficient sound absorbing materials.

[1]This paper presents preliminary results of an extended comprehensive work submitted to *Applied Acoustics*.

[2]tzielins@ippt.pan.pl

1. INTRODUCTION

Various AM technologies [1–3] are widely used recently to develop new acoustic materials and metamaterials [4–9], despite the fact that popular, inexpensive AM devices allow the formation of designed microstructures in relatively low resolution compared to the characteristic sizes found in efficient, conventional, sound-absorbing materials. Although the reproducibility of 3D printed porous sound absorbers has been recently confirmed through round robin tests involving various technologies, input materials, and 3D printers [10], manufacturing imperfections related to these technologies have been identified as a serious impediment when designing and prototyping such acoustic solutions. However, it has also been shown that some of these imperfections – unless they significantly alter the engineered geometry – may enhance acoustic properties. A good example here is the surface roughness, typical of many AM technologies, which usually increases a little the sound absorption of the 3D printed porous material thanks to the enhancement of dissipation associated with viscous effects [10, 11]. This work shows that another significant imperfection, namely porosity or rather microporosity, common with some AM technologies using powder as raw input material [12–14], can under certain conditions be used to 3D print materials with strongly enhanced sound-absorbing properties due to the double porosity thus realised.

The outline of this paper is as follows. The design and manufacturing of samples with a periodic pore network, as well the results of their microscopic examination are discussed in Section 2.1. This section also presents the results of direct measurements of the relevant properties of the 3D printed microporous material. Theoretical considerations and the necessary formulas for rigorous modelling related to the microstructure and sound-absorbing properties of the investigated materials are discussed in Section 2.2. Section 2.3 provides an overview and comparison of the measurement and modelling results. The main findings and conclusions are summarised in Section 3.

2. INVESTIGATIONS

2.1. Design and manufacturing

A simple periodic network of spherical pores was designed and used to 3D print acoustic samples in two different AM technologies: one technology produces a microporous skeleton leading to double porosity, while the other provides a single-porosity material with an impermeable skeleton. In this way, the double-porosity material should have the same main pore network as its single-porosity counterpart, allowing for a comparative analysis of acoustic efficiency, quantified through their sound absorbing properties.

The representative elementary volume (REV) containing the periodic main pore network is presented in Figure 1. It is a cubic cell of size $\ell_\mathrm{p} = 4\,\mathrm{mm}$, containing a single spherical pore with a diameter $d_\mathrm{sp} = 0.9\ell_\mathrm{p} = 3.6\,\mathrm{mm}$. The pore is directly connected with six neighbouring pores from the adjacent cells by two vertical and four horizontal channels, all of them cylindrical with the same

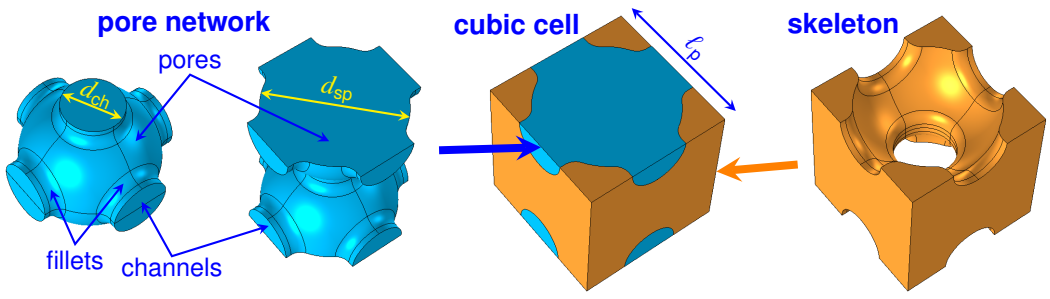

Figure 1: Periodic REV in the form of a cubic cell composed of complementary parts of the periodic pore network (blue) and microporous or solid skeleton (orange).

diameter $d_{ch} = 0.4\ell_p = 1.6\,\text{mm}$. Note that the periodic cubic cell shown in Figure 1 is periodically shifted so that it actually contains two separate pore halves connected by the vertical channel. The connections between each pore and the channels are rounded with a fillet radius of $r_f = 0.25 d_{ch}$. The porosity associated with such a main pore network will be denoted by ϕ_p. Its nominal, i.e. designed, value $\phi_p = 44.1\%$ will be corrected for actual 3D printed samples.

A computer-aided design (CAD) model of a cylindrical sample with a diameter of 31 mm (i.e. 2 mm larger than the target value) and height $H = 9\ell_p = 36\,\text{mm}$ was virtually cut out from a three-dimensional array of $8 \times 8 \times 9$ representative skeletal cells, see Figure 2. This model was used to 3D print samples using two different AM technologies: (i) Binder Jetting 3D printing (BJP) [2] – from a gypsum-based powder bounded with butyrolactam, and (ii) Stereolithography (SLA) [3] – from a photopolymer resin. The diameter of each 3D printed sample was tightly trimmed to perfectly fit the impedance tube of diameter $D_t = 29\,\text{mm}$, see Figure 2.

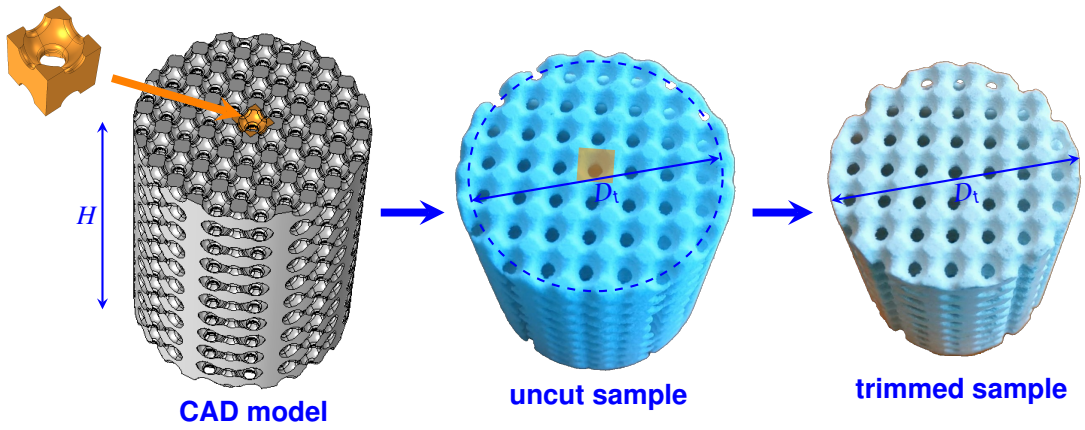

Figure 2: CAD model used to 3D print samples and the corresponding gypsum sample before and after it has been trimmed to fit perfectly into the impedance tube.

The flat surfaces of both samples were examined under a microscope (see Figure 3) to find that the quality of the resin sample is very good with all shapes very well mapped and all surfaces smooth, while the surfaces of the gypsum sample are rather rough and in the photography it is even difficult to

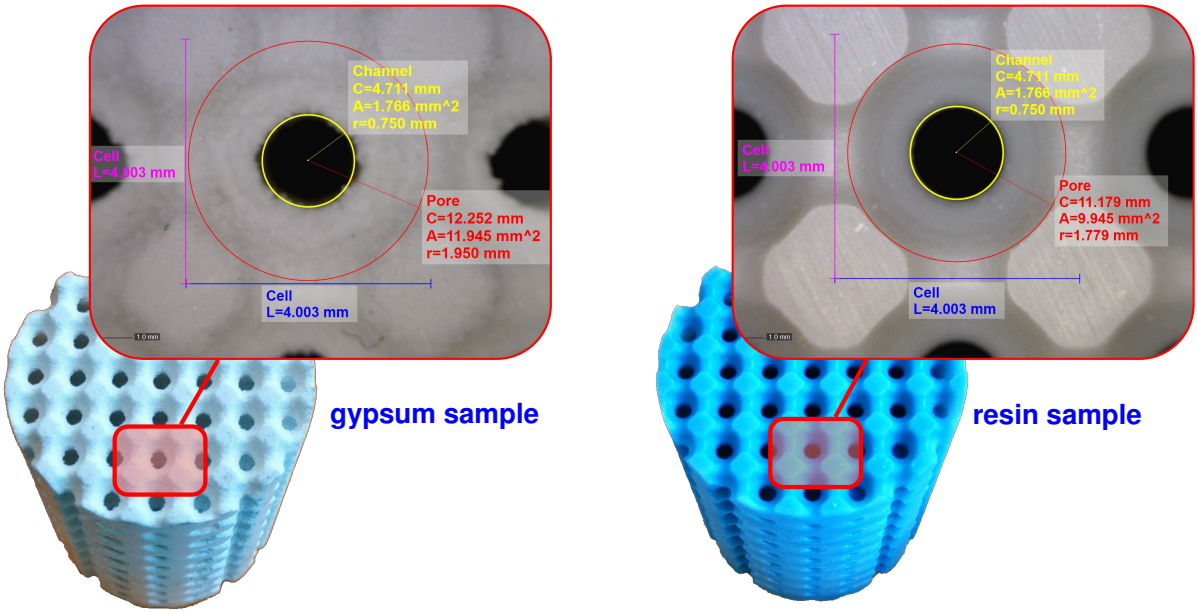

Figure 3: Microscopically examined surfaces of the 3D printed double-porosity gypsum sample (left) and single-porosity resin sample (right).

precisely define the actual shape and size of the pore. Nevertheless, in both cases the actual diameter of the channel can be reliably determined as $d_{\mathrm{ch}} = 1.50\,\mathrm{mm}$, which means that it is reduced by 0.1 mm from the value present in the CAD model used for 3D printing. The pore size in the resin sample is also accurately determined as $d_{\mathrm{sp}} = 3.56\,\mathrm{mm}$, so it is only slightly smaller than the nominal pore diameter in the CAD model, while the pore in the gypsum sample appears to be slightly larger and its actual diameter can be estimated as $d_{\mathrm{sp}} \approx 3.9\,\mathrm{mm}$. These actual values were used to update the designed geometry of the periodic REVs that are used for numerical calculations during the modelling (see Sections 2.2 and 2.3).

The results of preliminary experiments suggested that the skeleton of the gypsum sample was microporous. Therefore, homogenous (i.e. without the main pore network) disc-shaped specimens were 3D printed from the gypsum-based power in BJP technology, using the same 3D printer, binder, and process parameters as those used for the periodic cylindrical sample. These specimens were used for direct measurements of their microporosity and airflow resistivity of this 3D printed material. The measured microporosity is $\phi_{\mathrm{m}} = 42.6\%$, while the airflow resistivity is $32.24\,\mathrm{MPa{\cdot}s/m^2}$. The latter means that the viscous permeability of the microporous material is $\mathcal{K}_{0\mathrm{m}} = 5.7 \cdot 10^{-13}\,\mathrm{m}^2$.

2.2. Modelling

Acoustic waves penetrating air-saturated porous media with open pore networks and rigid frames induce harmonic flow and pressure fluctuations in the pores [15–18]. These phenomena are described by the complex amplitudes of the flux velocity $\mathbf{V}$ and pressure p. Assuming the time-harmonic convention $\exp(+\mathrm{i}\omega t)$, where i is the imaginary unit, ω is the angular frequency, and t denotes time, the wave propagation in such media can be described by the effective model comprising the macroscopic mass balance equation and dynamic Darcy's law [15], viz.

$$\nabla \cdot \mathbf{V} + \mathrm{i}\omega\, C_{\mathrm{e}}(\omega)\, p = 0\,, \qquad \mathbf{V} = -\frac{\mathcal{K}_{\mathrm{e}}(\omega)}{\eta}\nabla p\,, \tag{1}$$

where η is the dynamic viscosity of air saturating the pores, while C_{e} and $\mathcal{K}_{\mathrm{e}}$ are the effective compressibility and dynamic viscous permeability, respectively. Isotropic porous media are considered here, so C_{e} and $\mathcal{K}_{\mathrm{e}}$ are complex-valued *scalar* functions of frequency. Other useful effective properties can be introduced, in particular the effective density ϱ_{e} and speed of sound c_{e}, i.e.

$$\varrho_{\mathrm{e}}(\omega) = \frac{\eta}{\mathrm{i}\omega\,\mathcal{K}_{\mathrm{e}}(\omega)}\,, \qquad c_{\mathrm{e}}(\omega) = \sqrt{\frac{\mathrm{i}\omega\,\mathcal{K}_{\mathrm{e}}(\omega)}{\eta\, C_{\mathrm{e}}(\omega)}}\,. \tag{2}$$

Eliminating $\mathbf{V}$ from Equation 1 leads to the classic Helmholtz equation for time-harmonic acoustics, viz. $\nabla^2 p + k_{\mathrm{e}}^2(\omega)\, p = 0$, where $k_{\mathrm{e}}(\omega) = \omega/c_{\mathrm{e}}(\omega)$ is the complex wave number in the effective fluid equivalent to the porous medium.

Single- and double-porosity materials are studied in this work and their effective properties (denoted above by the subscript 'e') as well as some specific parameters are distinguished below with the subscripts 'p' or 'db', respectively. The main difference between these two material types is the skeleton which can be impervious or microporous, and in the latter case, together with the main pore network, creates a double porosity material with highly contrasted permeabilities. The parameters and effective properties associated with the microporous material of the skeleton are denoted by the subscript 'm'.

The dynamic viscous permeability $\mathcal{K}_{\mathrm{p}}$ for a single-porosity medium with open porosity ϕ_{p} can be determined using the well-known scaling function of the so-called Johnson-Champoux-Allard-Lafarge-Pride (JCALP) model [15, 19–22], viz.

$$\mathcal{K}_{\mathrm{p}}(\omega) = \mathcal{K}_{0\mathrm{p}}\left(\frac{\mathrm{i}\omega}{\omega_{\mathrm{vp}}} + 1 - \mathcal{P}_{\mathrm{vp}} + \sqrt{\mathcal{P}_{\mathrm{vp}}^2 + \frac{\mathcal{M}_{\mathrm{vp}}}{2}\frac{\mathrm{i}\omega}{\omega_{\mathrm{vp}}}}\right)^{-1}\,, \qquad \omega_{\mathrm{vp}} = \frac{\phi_{\mathrm{p}}\,\nu}{\mathcal{K}_{0\mathrm{p}}\,\alpha_{\infty\mathrm{p}}}\,, \tag{3}$$

where $\mathcal{K}_{0\mathrm{p}} \equiv \mathcal{K}_{\mathrm{p}}(0)$ is the static viscous permeability, ω_{vp} is the Biot frequency, while $\mathcal{M}_{\mathrm{vp}} = 8\mathcal{K}_{0\mathrm{p}}\alpha_{\infty\mathrm{p}}/(\phi_{\mathrm{p}}\,\Lambda_{\mathrm{vp}}^2)$ and $\mathcal{P}_{\mathrm{vp}} = 0.25\mathcal{M}_{\mathrm{vp}}\alpha_{\infty\mathrm{p}}/(\alpha_{0\mathrm{vp}} - \alpha_{\infty\mathrm{p}})$ are the corresponding shape factors. Moreover, ν is the kinematic viscosity of air saturating the pores, and the remaining parameters are the (kinematic) tortuosity $\alpha_{\infty\mathrm{p}}$, static viscous tortuosity $\alpha_{0\mathrm{vp}}$, and viscous characteristic length Λ_{vp}. Five real-valued parameters associated with the pore network are required to calculate the complex-valued function $\mathcal{K}_{\mathrm{p}}(\omega)$, i.e. ϕ_{p}, $\mathcal{K}_{0\mathrm{p}}$, Λ_{vp}, $\alpha_{\infty\mathrm{p}}$ and $\alpha_{0\mathrm{vp}}$. These can be determined directly from the pore geometry (ϕ_{p}) or by solving the specific Stokes' flow ($\mathcal{K}_{0\mathrm{p}}$, $\alpha_{0\mathrm{vp}}$) and Laplace's problem (Λ_{vp}, $\alpha_{\infty\mathrm{p}}$) formulated in the pore space of the periodic REV [18, 23, 24]

The effective compressibility C_{p} for single-porosity media is calculated as

$$C_{\mathrm{p}}(\omega) = \frac{\phi_{\mathrm{p}}}{P_0}\left(1 - \frac{\gamma - 1}{\gamma}\frac{\Theta_{\mathrm{p}}(\omega)}{\Theta_{0\mathrm{p}}}\frac{\mathrm{i}\omega}{\omega_{\mathrm{tp}}}\right), \tag{4}$$

where P_0 is the ambient mean pressure and γ is the adiabatic index for air, while the so-called dynamic thermal permeability Θ_{p} can be determined from the scaling function of the JCALP model, i.e.

$$\Theta_{\mathrm{p}}(\omega) = \Theta_{0\mathrm{p}}\left(\frac{\mathrm{i}\omega}{\omega_{\mathrm{tp}}} + 1 - \mathcal{P}_{\mathrm{tp}} + \sqrt{\mathcal{P}_{\mathrm{tp}}^2 + \frac{\mathcal{M}_{\mathrm{tp}}}{2}\frac{\mathrm{i}\omega}{\omega_{\mathrm{tp}}}}\right)^{-1}, \qquad \omega_{\mathrm{tp}} = \frac{\phi_{\mathrm{p}}\,\tau}{\Theta_{0\mathrm{p}}}, \tag{5}$$

where $\Theta_{0\mathrm{p}} \equiv \Theta_{\mathrm{p}}(0)$ is the static thermal permeability, ω_{tp} is the thermal characteristic frequency, while $\mathcal{M}_{\mathrm{tp}} = 8\Theta_{0\mathrm{p}}/(\phi_{\mathrm{p}}\,\Lambda_{\mathrm{tp}}^2)$ and $\mathcal{P}_{\mathrm{tp}} = 0.25\mathcal{M}_{\mathrm{tp}}/(\alpha_{0\mathrm{tp}} - 1)$ are the corresponding shape factors. Moreover, τ is the thermal diffusivity of air, while the remaining parameters are the static thermal tortuosity $\alpha_{0\mathrm{tp}}$ and thermal characteristic length Λ_{tp}. Four real-valued parameters associated with the pore network are required to calculate the complex-valued function $\Theta_{\mathrm{p}}(\omega)$, i.e. ϕ_{p}, $\Theta_{0\mathrm{p}}$, Λ_{tp}, and $\alpha_{0\mathrm{tp}}$. These can be determined directly from the pore geometry (ϕ_{p}, Λ_{tp}) or by solving the specific Poisson's problem ($\Theta_{0\mathrm{tp}}$, $\alpha_{0\mathrm{tp}}$) formulated in the pore space of the periodic REV [18, 23, 24].

The microporous material is a specific single-porosity case. Therefore, its effective properties can determined from the formulas presented above, where the subscript 'p' is replaced with 'm', which means that all macro-parameters are determined for the microporous network. However, due to the fact that the micropores are by definition very small, one can expect that in the frequency range of interest, e.g. up to 6.4 kHz, the dynamic viscous permeability $\mathcal{K}_{\mathrm{m}}$ and effective compressibility C_{m} are practically constant and equal to their (real-valued) static counterparts, i.e. $\mathcal{K}_{\mathrm{m}}(\omega) \approx \mathcal{K}_{\mathrm{m}}(0) \equiv \mathcal{K}_{0\mathrm{m}}$ and $C_{\mathrm{m}}(\omega) \approx C_{\mathrm{m}}(0) \equiv C_{0\mathrm{m}} = \phi_{\mathrm{m}}/P_0$. It is therefore sufficient to determine only the static viscous permeability $\mathcal{K}_{0\mathrm{m}}$ and porosity ϕ_{m} of the microporous material, and these properties were measured directly for disc-shaped material specimens 3D printed from the gypsum powder (see Section 2.1).

In this study, high permeability contrast is assumed between the main pore network and the microporous skeleton, i.e. $\mathcal{K}_{0\mathrm{p}} \gg \mathcal{K}_{0\mathrm{m}}$, which means that visco-inertial flow is restricted mainly to the main pores and the dynamic viscous permeability $\mathcal{K}_{\mathrm{db}}$ for such double-porosity materials can be determined as for their single-porosity counterparts, i.e. $\mathcal{K}_{\mathrm{db}}(\omega) \approx \mathcal{K}_{\mathrm{p}}(\omega)$. Still, the effective compressibility C_{db} depends not only on the air compression and the associated heat dissipation effects in the main pore network, but also on those in the microporous skeleton. Moreover, an additional dissipation effect may occur due to the fact that two local acoustic pressure fields can coexist, namely a locally constant pressure field in the more permeable pore network and a pressure field that varies locally in the less permeable microporous skeleton, which ultimately leads to pressure diffusion that provides additional sound energy dissipation. Therefore, the effective compressibility C_{db} for a double-porosity material [16, 17] is calculated as

$$C_{\mathrm{db}}(\omega) = C_{\mathrm{p}}(\omega) + \phi_{\mathrm{d}}\,C_{0\mathrm{m}}\,\mathcal{F}_{\mathrm{d}}(\omega), \qquad \mathcal{F}_{\mathrm{d}}(\omega) = 1 - \frac{\mathcal{B}_{\mathrm{d}}(\omega)}{\mathcal{B}_{0\mathrm{d}}}\frac{\mathrm{i}\omega}{\omega_{\mathrm{d}}}. \tag{6}$$

where $\phi_{\mathrm{d}} = 1 - \phi_{\mathrm{p}}$ is the volume fraction of the microporous skeleton and $\mathcal{F}_{\mathrm{d}}$ is the ratio of the averaged pressure locally fluctuating in the microporous domain to the pressure in the main pores [16, 17]. The

latter depends on the so-called dynamic pressure diffusion function $\mathcal{B}_\mathrm{d}$ which can be determined using the scaling function as

$$\mathcal{B}_\mathrm{d}(\omega) = \mathcal{B}_{0\mathrm{d}} \left(\frac{\mathrm{i}\omega}{\omega_\mathrm{d}} + 1 - \mathcal{P}_\mathrm{d} + \sqrt{\mathcal{P}_\mathrm{d}^2 + \frac{\mathcal{M}_\mathrm{d}}{2} \frac{\mathrm{i}\omega}{\omega_\mathrm{d}}} \right)^{-1}, \qquad \omega_\mathrm{d} = \frac{\phi_\mathrm{d}\, \mathcal{D}_{0\mathrm{m}}}{\mathcal{B}_{0\mathrm{d}}}, \tag{7}$$

where $\mathcal{B}_{0\mathrm{d}} \equiv \mathcal{B}_\mathrm{d}(0)$ is the static pressure diffusion, ω_d is the pressure diffusion characteristic frequency, while $\mathcal{M}_\mathrm{d} = 8\mathcal{B}_{0\mathrm{d}}/(\phi_\mathrm{d}\, \Lambda_\mathrm{d}^2)$ and $\mathcal{P}_\mathrm{d} = 0.25\mathcal{M}_\mathrm{d}/(\alpha_{0\mathrm{d}} - 1)$ are the corresponding shape factors. Here, the so-called static pressure diffusivity of microporous material $\mathcal{D}_{0\mathrm{m}} = \mathcal{K}_{0\mathrm{m}}/(\eta\, C_{0\mathrm{m}})$ is introduced, and two additional parameters related to the pressure diffusion occurring in the microporous domain are the corresponding static tortuosity $\alpha_{0\mathrm{d}}$ and characteristic length Λ_d. Four real-valued parameters associated with the microporous domain are required to calculate the complex-valued function $\mathcal{B}_\mathrm{d}(\omega)$, i.e. ϕ_d, $\mathcal{B}_{0\mathrm{d}}$, Λ_d, and $\alpha_{0\mathrm{d}}$. These can be determined directly from the domain's geometry (ϕ_d, Λ_d) or by solving the specific Poisson's problem ($\mathcal{B}_{0\mathrm{d}}$, $\alpha_{0\mathrm{d}}$) formulated in the microporous domain of the periodic REV [16, 17].

When the dynamic viscous permeability and effective compressibility as well as other useful effective properties (see Equation 2) have been determined for porous media with micro-, single- or double-porosity, the sound absorption coefficient $\mathcal{A}$ at normal incidence can be calculated (from the solution of the relevant Helmholtz problem) for a porous layer of a specified thickness H, made of one of the determined materials and backed by a rigid wall or, alternatively, by an air gap of a thickness H_g between the wall and porous layer. For this purpose, the surface acoustic impedance [15] is first determined as

$$Z_\mathrm{s}(\omega) = \begin{cases} -\mathrm{i}\, Z_\mathrm{e}(\omega) \cot\left(H k_\mathrm{e}(\omega)\right) & \text{for a porous layer backed by a rigid wall,} \\ Z_\mathrm{e}(\omega) \dfrac{Z_\mathrm{e}(\omega) - \mathrm{i}\, Z_\mathrm{g}(\omega) \cot\left(H k_\mathrm{e}(\omega)\right)}{Z_\mathrm{g}(\omega) - \mathrm{i}\, Z_\mathrm{e}(\omega) \cot\left(H k_\mathrm{e}(\omega)\right)} & \text{for a porous layer backed by an air gap.} \end{cases} \tag{8}$$

Here, $Z_\mathrm{e}(\omega) = \varrho_\mathrm{e}(\omega)\, c_\mathrm{e}(\omega)$ is the effective characteristic impedance of the porous material of the layer and $Z_\mathrm{g}(\omega) = -\mathrm{i}\, Z_0 \cot\left(H_\mathrm{g}\omega/c_0\right)$ is the impedance of the air gap, where c_0 and Z_0 are the speed of sound and characteristic impedance of air, respectively. Then, the acoustic reflection coefficient $\mathcal{R}(\omega) = \left(Z_\mathrm{s}(\omega) - Z_0\right)/\left(Z_\mathrm{s}(\omega) + Z_0\right)$ and sound absorption $\mathcal{A}(\omega) = 1 - \left|\mathcal{R}(\omega)\right|^2$ are calculated [15].

2.3. Results and discussion

To discuss the nature of the manufactured materials, the experimental results will be compared with the corresponding predictions obtained from numerical modelling. Therefore, the air properties used in calculations were determined for the ambient conditions of pressure ($P_0 = 996.3$ hPa), temperature (27.6°C), and relative humidity (53%), found during the experimental tests in the impedance tube.

Table 1 shows parameters calculated numerically from the periodic REVs with geometries updated thanks to microscopic examination of real samples. These updates were a little different for the gypsum sample and for the resin sample, so the visco-inertial and thermal parameters calculated for

Table 1: Parameters calculated numerically for the gypsum (BJP) and resin (SLA) samples.

	Visco-inertial effects					Thermal effects				Pressure diffusion			
	ϕ_p	$\mathcal{K}_{0\mathrm{p}}$	Λ_vp	$\alpha_{0\mathrm{vp}}$	$\alpha_{\infty\mathrm{p}}$	ϕ_p	$\Theta_{0\mathrm{p}}$	Λ_tp	$\alpha_{0\mathrm{tp}}$	ϕ_d	$\mathcal{B}_{0\mathrm{d}}$	Λ_d	$\alpha_{0\mathrm{d}}$
	%	$10^{-8}\mathrm{m}^2$	mm	–	–	%	$10^{-8}\mathrm{m}^2$	mm	–	%	$10^{-8}\mathrm{m}^2$	mm	–
BJP	50.7	2.66	0.862	2.65	1.88	50.7	14.4	1.56	1.36	49.3	11.9	1.52	1.36
SLA	42.3	2.10	0.850	2.59	1.87	42.3	9.86	1.40	1.38	—	—	—	—

one sample differ slightly from those calculated for the other. The parameters associated with the pressure diffusion were calculated only for the gypsum sample which has a microporous skeleton.

The parameters listed in Table 1 were used to determine the effective properties for both samples as discussed in Section 2.2. In particular, to compute the effective compressibility for the double-porosity gypsum sample, the pressure ratio function $\mathcal{F}_\mathrm{d}(\omega)$ was determined, see Figure 4. This function indicates whether pressure diffusion takes place and over what frequency range this effect is strong. The pressure diffusion is present at frequencies where the function $\mathcal{F}_\mathrm{d}$ is essentially complex-valued, which means that there is a phase shift between the pressure in the main pore network and the micropores, leading to increased dissipation of acoustic energy. Figure 4 shows that pressure diffusion becomes significant around 1 kHz and above, reaching its maximum around the characteristic frequency $f_\mathrm{d} = \omega_\mathrm{d}/(2\pi) = 4.75$ kHz. The pressure diffusion becomes weak below 1 kHz and very weak below 600–700 Hz.

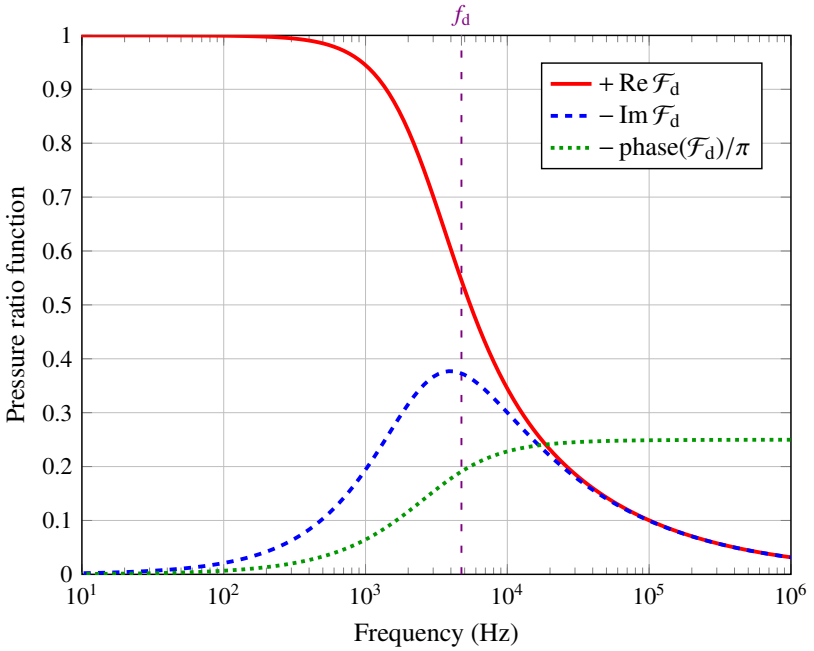

Figure 4: The frequency-dependent ratio $\mathcal{F}_\mathrm{d}$ of the averaged pressure in the micropores to the pressure in the main pores of the periodic cell, responsible for pressure diffusion in the gypsum sample with double porosity.

The sound absorption coefficient of both samples was measured in an impedance tube, for frequencies up to 6.4 kHz. The samples were backed by a rigid piston closing the tube, but in addition, the measurements were also carried out with an air gap of thickness $H_\mathrm{g} = 44$ mm between the rear face of the sample and the piston. The results are compared in Figure 5 with the corresponding predictions calculated as explained in Section 2.2. Sound absorption predictions were also shown for a microporous layer of the same thickness $H = 36$ mm as the height of the samples, to show that this absorption is very poor and that such microporous materials can only be acoustically efficient when used as constituents in double-porosity solutions. This is actually demonstrated here by comparison of the corresponding absorption curves measured (and, in fact, very well predicted) for the double-porosity gypsum sample and the single-porosity resin sample. It becomes evident that the presence of micropores in the skeleton of the gypsum sample produces strong additional dissipation effects related mainly to pressure diffusion. In general, the sound absorption in the double-porosity material – when compared with the results obtained for the single-porosity material with the same (or very similar) main pore network – is much better in almost the entire frequency range: the absorption peaks are shifted to lower frequencies and the sound absorption between them is significantly increased. Specifically, the results found for porous layers (samples) backed by a rigid

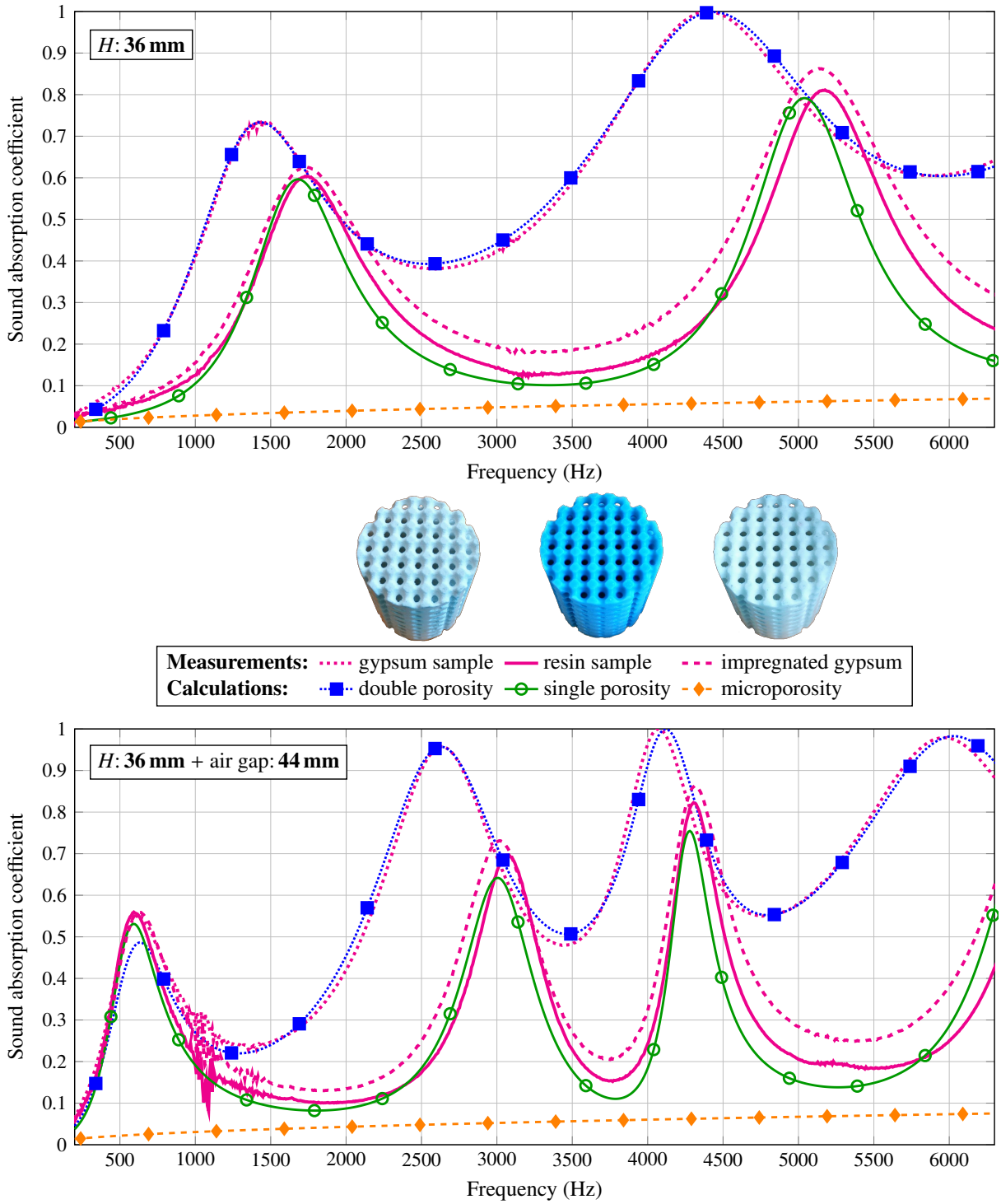

Figure 5: Sound absorption measured and calculated for the gypsum sample with double porosity and for the single-porosity resin and impregnated gypsum samples, backed by a rigid wall (upper graph) or by an air gap (lower graph), also the corresponding sound absorption predictions for a microporous layer of the same thickness as the 3D printed samples.

wall (piston), shown in the upper graph in Figure 5, reveal that the first absorption peak has been improved: from 0.6 at about 1.7 kHz (single-porosity material) to 0.73 at 1.4 kHz (double-porosity material). However, when each porous layer is backed by the air gap (so that the total thickness of such a double layer is 80 mm), the first absorption peak is very similar for both samples (see the lower graph in Figure 5), as it has been shifted to much lower frequency of about 600 Hz, where the pressure diffusion effect is weak (see Figure 4).

To show that such a significant improvement in sound absorption is mainly achieved due to the double porosity, the gypsum sample was impregnated with cyanoacrylate in order to close the micropores in its skeleton, making it a single-porosity material. Then, the impregnated sample was tested again to find that the corresponding absorption curves are very similar to the ones obtained for the *single-porosity* resin sample, although with noticeably, but not significantly, greater absorption between the peaks (see Figure 5). The latter can be attributed to the fact that the skeleton surfaces of the gypsum sample are rough as opposed to the perfectly smooth surfaces of the resin sample, and thus, the viscous dissipation effects are slightly increased in the gypsum specimen.

3. CONCLUSIONS

Prototypes of efficient acoustic materials with double porosity can be designed and easily manufactured with some low-cost AM technologies using powders as raw input materials and allowing inherent microporosity. This is because the appropriate high permeability contrast between the 3D printed microporous skeleton and the designed main pore network can be readily achieved, leading to the phenomenon of pressure diffusion which is an additional, efficient sound energy dissipation mechanism. These observations have been proven in dedicated experimental tests combined with rigorous multi-scale modelling which gives accurate predictions provided that the microporosity and airflow resistivity of the microporous skeleton have been determined, e.g. with direct measurements, and the real sizes and shapes of the designed pore network are known. In practice, the designed geometry can be updated on the basis of microscopic examination of samples or – in some cases – from the 3D printer user's experience acquired in this way. All this opens up great prospects for the design and prototyping of innovative acoustic materials.

ACKNOWLEDGEMENTS

T. G. Zielinski acknowledges the financial support from the project "Sound-absorbing composites: coupled acoustic energy dissipation mechanisms, multiscale modelling and prototyping", financed under Grant Agreement No. 2021/41/B/ST8/04492 by the National Science Centre (NCN), Poland. R. Venegas acknowledges support from the Chilean National Agency for Research and Development (ANID) through FONDECYT Grant No. 1211310.

REFERENCES

[1] I. Gibson, D. Rosen, and B. Stucker. *Additive Manufacturing Technologies: 3D Printing, Rapid Prototyping, and Direct Digital Manufacturing*. Springer, New York, 2 edition, 2015.

[2] A. Mostafaei, A. M. Elliott, J. E. Barnes, F. Li, W. Tan, C. L. Cramer, P. Nandwana, and M. Chmielus. Binder jet 3D printing—Process parameters, materials, properties, modeling, and challenges. *Progress in Materials Science*, 119:100707, 2021.

[3] F. Zhang, L. Zhu, Z. Li, S. Wang, J. Shi, W. Tang, N. Li, and J. Yang. The recent development of vat photopolymerization: A review. *Additive Manufacturing*, 48:102423, 2021.

[4] K. C. Opiela and T. G. Zieliński. Microstructural design, manufacturing and modelling of an adaptable porous composite sound absorber. *Composites Part B: Engineering*, 187:107833, 2020.

[5] J. Boulvert, J. Costa-Baptista, T. Cavalieri, M. Perna, E. R. Fotsing, V. Romero-García, G. Gabard, A. Ross, J. Mardjono, and J.-P. Groby. Acoustic modeling of micro-lattices obtained by additive manufacturing. *Applied Acoustics*, 164:107244, 2020.

[6] H. J. Rice, J. Kennedy, P. Göransson, L. Dowling, and D. Trimble. Design of a Kelvin cell acoustic metamaterial. *Journal of Sound and Vibration*, 472:115167, 2020.

[7] L. Suárez and M. del Mar Espinosa. Assessment on the use of additive manufacturing technologies for acoustic applications. *The International Journal of Advanced Manufacturing Technology*, 109:2691–2705, 2020.

[8] J. Carbajo, J. M. Molina-Jordá, L. P. Maiorano, and N. X. Fang. Sound absorption of macro-perforated additively manufactured media. *Applied Acoustics*, 182:108204, 2021.

[9] W. Johnston and B. Sharma. Additive manufacturing of fibrous sound absorbers. *Additive Manufacturing*, 41:101984, 2021.

[10] T. G. Zieliński, K. C. Opiela, P. Pawłowski, N. Dauchez, T. Boutin, J. Kennedy, D. Trimble, H. Rice, B. Van Damme, G. Hannema, R. Wróbel, S. Kim, S. Ghaffari Mosanenzadeh, N. X. Fang, J. Yang, B. Briere de La Hosseraye, M. C. J. Hornikx, E. Salze, M.-A. Galland, R. Boonen, A. Carvalho de Sousa, E. Deckers, M. Gaborit, and J.-P. Groby. Reproducibility of sound-absorbing periodic porous materials using additive manufacturing technologies: Round robin study. *Additive Manufacturing*, 36:101564, 2020.

[11] J. Kennedy, L. Flanagan, L. Dowling, G. J. Bennett, H. Rice, and D. Trimble. The influence of additive manufacturing processes on the performance of a periodic acoustic metamaterial. *International Journal of Polymer Science*, 2019:7029143, 2019.

[12] A. du Plessis. Effects of process parameters on porosity in laser powder bed fusion revealed by X-ray tomography. *Additive Manufacturing*, 30:100871, 2019.

[13] R. J. Williams, A. Piglione, T. Rønneberg, C. Jones, M.-S. Pham, C. M. Davies, and P. A. Hooper. In situ thermography for laser powder bed fusion: Effects of layer temperature on porosity, microstructure and mechanical properties. *Additive Manufacturing*, 30:100880, 2019.

[14] L. Dowling, J. Kennedy, S. O'Shaughnessy, and D. Trimble. A review of critical repeatability and reproducibility issues in powder bed fusion. *Materials and Design*, 186:108346, 2020.

[15] J. F. Allard and N. Atalla. *Propagation of Sound in Porous Media: Modeling Sound Absorbing Materials, Second Edition*. John Wiley & Sons, Chichester, 2009.

[16] C. Boutin, P. Royer, and J. L. Auriault. Acoustic absorption of porous surfacing with dual porosity. *International Journal of Solids and Structures*, 35:4709–4737, 1998.

[17] X. Olny and C. Boutin. Acoustic wave propagation in double porosity media. *The Journal of the Acoustical Society of America*, 114:73–89, 2003.

[18] T. G. Zieliński, R. Venegas, C. Perrot, M. Červenka, F. Chevillotte, and K. Attenborough. Benchmarks for microstructure-based modelling of sound absorbing rigid-frame porous media. *Journal of Sound and Vibration*, 483:115441, 2020.

[19] D. L. Johnson, J. Koplik, and R. Dashen. Theory of dynamic permeability and tortuosity in fluid-saturated porous media. *Journal of Fluid Mechanics*, 176:379–402, 1987.

[20] Y. Champoux and J.-F. Allard. Dynamic tortuosity and bulk modulus in air-saturated porous media. *Journal of Applied Physics*, 70:1975–1979, 1991.

[21] D. Lafarge, P. Lemarinier, J. F. Allard, and V. Tarnow. Dynamic compressibility of air in porous structures at audible frequencies. *The Journal of the Acoustical Society of America*, 102:1995–2006, 1997.

[22] S. R. Pride, F. D. Morgan, and A. F. Gangi. Drag forces of porous-medium acoustics. *Physical Review B*, 47:4964–4978, 1993.

[23] S. Gasser, F. Paun, and Y. Bréchet. Absorptive properties of rigid porous media: Application to face centered cubic sphere packing. *The Journal of the Acoustical Society of America*, 117:2090–2099, 2005.

[24] C. Perrot, F. Chevillotte, and R. Panneton. Bottom-up approach for microstructure optimization of sound absorbing materials. *The Journal of the Acoustical Society of America*, 124:940–948, 2008.